Bull. Seismological Soc. Amer., 93 (4), 1803-1822, 2003.

Anisotropic Changes in P-Wave Velocity and Attenuation During Deformation and Fluid Infiltration of Granite

Sergei A. Stanchits[123]
David A. Lockner[2]
and
Alexander V. Ponomarev[4]

Abstract. Fluid infiltration and pore fluid pressure changes are known to have a significant effect on the occurrence of earthquakes. Yet, for most damaging earthquakes, with nucleation zones below a few kilometers depth, direct measurements of fluid pressure variations are not available. Instead, pore fluid pressures are inferred primarily from seismic wave propagation characteristics such as V_p/V_s ratio, attenuation and reflectivity contacts. We present laboratory measurements of changes in P-wave velocity and attenuation during the injection of water into a granite sample as it was loaded to failure. A cylindrical sample of Westerly granite was deformed at constant confining and pore pressures of 50 and 1 MPa respectively. Axial load was increased in discrete steps by controlling axial displacement. Anisotropic P-wave velocity and attenuation fields were determined during the experiment using an array of 13 piezoelectric transducers. At the final loading steps (86 and 95 percent of peak stress), both spatial and temporal changes in P-wave velocity and peak-to-peak amplitudes of P- and S-waves were observed. P-wave velocity anisotropy reached a maximum of 26%. Transient increases in attenuation of up to 483 dB/meter were also observed and were associated with diffusion of water into the sample. We show that velocity and attenuation of P-waves are sensitive to the process of opening of microcracks and the subsequent resaturation of these cracks as water diffuses in from the surrounding region. Symmetry of the orientation of newly formed microcracks results in anisotropic velocity and attenuation fields which systematically evolve in response to changes in stress and influx of water. With proper scaling, these measurements provide constraints on the magnitude and duration of velocity and attenuation transients that can be expected to accompany the nucleation of earthquakes in the earth's crust.

Introduction

Numerous models have been proposed for the temporal variation of seismic velocities expected to occur prior to an earthquake. Many of these models (e.g., the Dilatancy-Diffusion model (Nur, 1972; Scholz *et al*., 1973)) are based on the observation that brittle failure of rock involves opening of cracks and volumetric change leading to an under-saturation of the nucleation zone followed by resaturation due to the influx of water from the surrounding rock. Consequently, the Dilatancy-Diffusion model predicted a decrease and then recovery of *V*p/*V*s velocity ratio in the nucleation zone prior to large earthquakes. Early enthusiasm for such models was based on field observations including anomalous phenomena before earthquakes, such as variations in longitudinal and transverse velocities (Semyonov, 1969; Robinson *et al*., 1972; Aggarwal *et al*., 1973; Whitcomb *et al*., 1973) and decrease in electric resistivity (Barsukov, 1970). However, such field observations have not occurred consistently before earthquakes and have not proven to be reliable prediction tools. Indeed, questions of non-time-stationary characteristics of source event populations and related sampling bias issues have shown how unintentional systematic errors might affect estimates of velocity (Lindh *et al*.,

[1] GeoForschungsZentrum Potsdam, GERMANY
[2] U.S. Geological Survey, Menlo Park, California, USA
[3] also at Physical-Technical Institute, Russian Academy of Sciences, St. Petersburg, RUSSIA
[4] Institute of Physics of the Earth, Russian Academy of Sciences, Moscow, RUSSIA
-3/2002 Submitted to *Bull. Seismological Society of America*
-3/2003 Accepted for publication.

1978; Lockner and Byerlee, 1978). At the same time, dilatancy during failure of brittle rock remains a well-known experimental fact that has been measured repeatedly in laboratory experiments (Brace *et al*., 1966; Scholz, 1968b; Zoback and Byerlee, 1975; Hadley, 1976; Tapponnier and Brace, 1976; Kranz and Scholz, 1977; Yanagidani *et al*., 1985; Sobolev, 1995; Lockner, 1998). Measurements on down-hole strain meters in the near field of moderate earthquakes indicate that nucleation zones may be less than 100 m across (Johnston *et al*., 1987; Linde and Johnston, 1989; Johnston *et al*., 1990; Johnston and Linde, 2002). Thus, it would be difficult to detect the small perturbations in total travel times of seismic waves passing through a small nucleation zone at depth. This may provide an explanation for the lack of field observations of fluid-driven velocity transients prior to earthquakes.

While precursory velocity changes have not been identified in field measurements, neither do we know of laboratory measurements that explicitly show the sequence of velocity decrease and then recovery predicted to occur when fluid diffuses into a stressed rock. Laboratory experiments have shown, through the migration of acoustic emission (AE) source events and associated microcracking that the infiltration of pore fluid under high pressure can lead to rock failure both in tension (Lockner and Byerlee, 1980) and in shear (Byerlee and Lockner, 1977; Kranz *et al*., 1990; Masuda *et al*., 1990; Masuda *et al*., 1993). These studies were all designed so that samples, which had been pre-loaded to near failure, would be induced to fail by reduction of effective confining pressure ($P_{c,\,eff} = P_c - p$, where P_c and p are applied confining and pore pressure, respectively) as high pressure water was injected into the pore space. Simultaneous measurements of both AE hypocenters and wave velocities showed the correlation between migration of the active AE zone and the position of the water front. Masuda *et al*. (1990) suggested a positive feedback mechanism of fracture in which the infiltration of water raised the pore pressure around a dilatant region where local strength had already decreased, resulting in further decreasing local strength. In the earth, we might expect that in highly stressed tectonic regions, fluid flow can play a critical role in triggering earthquakes. Increasing fluid pressure may advance the timing of earthquakes (Miller *et al*., 1996) or contribute to the breakdown of strength (Blanpied *et al*., 1992). Conversely, dilatancy hardening of fluid-saturated rock can delay the onset of instability (Lockner and Byerlee, 1994, 1995; Lockner and Stanchits, 2002 in press). Therefore, laboratory experiments under conditions of known stress and fluid pressure may provide useful observations of the types of precursory changes that could occur.

Numerous laboratory studies (e.g., Nur and Simmons (1969), Bonner (1974) and Lockner *et al*. (1977)) have shown the development of strong velocity and attenuation anisotropy in dry rock loaded to failure as microcracks orientated sub-parallel to the maximum compressive principal stress are opened. These microcracks are responsible for the dilatancy and reduction in P-wave velocity that precedes brittle failure in rock (Sobolev, 1995). Yukutake (1989; 1992) has reported the development of significant velocity heterogeneity in dry granite samples within a few percent of peak stress, lending support to the observations of AE localization associated with fault nucleation (Lockner *et al*., 1991, 1992a; Lockner *et al*., 1992b; Moore and Lockner, 1995). The fluid injection studies mentioned above (Kranz *et al*., 1990; Masuda *et al*., 1993) have shown a time-dependent velocity recovery for the slow P-wave direction (perpendicular to the maximum stress direction) as water diffuses into the sample and fills open microcracks. In the present study we, too, have loaded a granite sample to failure in discrete steps. However, significant differences have been incorporated into our experiments, including (a) low and constant pore pressure (1 MPa) applied to the ends of the sample, allowing for undersaturation and then resaturation to occur within the sample; (b) measurement of spatial and temporal variation of the full P-wave velocity and attenuation fields; (c) large sample size; and (d) time sequences showing the complete velocity loss/recovery sequence for comparison with the Dilatancy -Diffusion model.

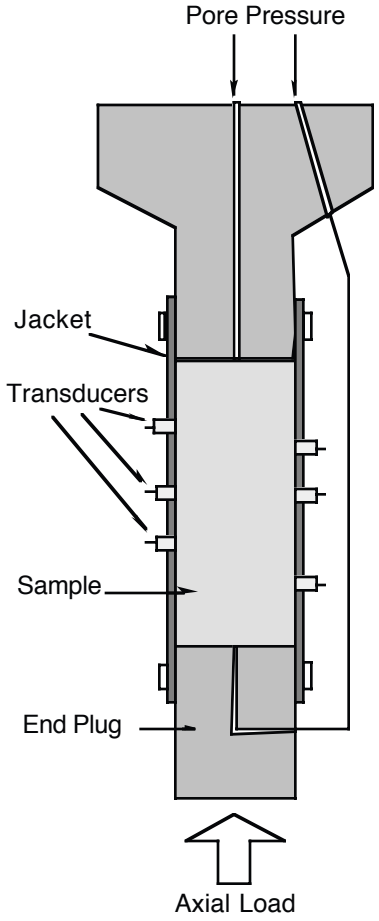

Figure 1. Schematic view of sample mounted in pressure vessel.

Experimental Procedure

A cylindrical sample of Westerly Granite, 190.5 mm long by 76.2 mm in diameter was placed between unlubricated steel endcaps, jacketed in a polyurethane sleeve and mounted in a triaxial deformation machine (see, for example, Lockner *et al*. (1992a)). Figure 1 shows a schematic view of the sample assembly. After being placed in the pressure vessel but prior to testing, the sample was first evacuated for 24 hours and then saturated with deionized water as follows. An external pore pressure control system was connected to the ends of the sample and water was injected at 1 MPa pressure. The water injection rate gradually dropped to zero at which time the sample was deemed saturated. The faces of the steel endcaps touching the sample were scribed with patterns consisting of six radial lines and a 50 mm-diameter circle to assist the distribution of water over the sample ends. Even so, because of the low permeability of Westerly granite (approximately 70 nDa ($7x10^{-20}$ m^2)) the saturation procedure took more than two days. Once fully saturated, the sample was deformed at room temperature and at constant confining pressure of P_C = 50.0±0.2 MPa and constant pore pressure of p = 1.0±0.05 MPa. Axial shortening was measured outside the pressure vessel by a DCDT displacement transducer with ±0.3 micron precision. Axial load was also measured outside the vessel

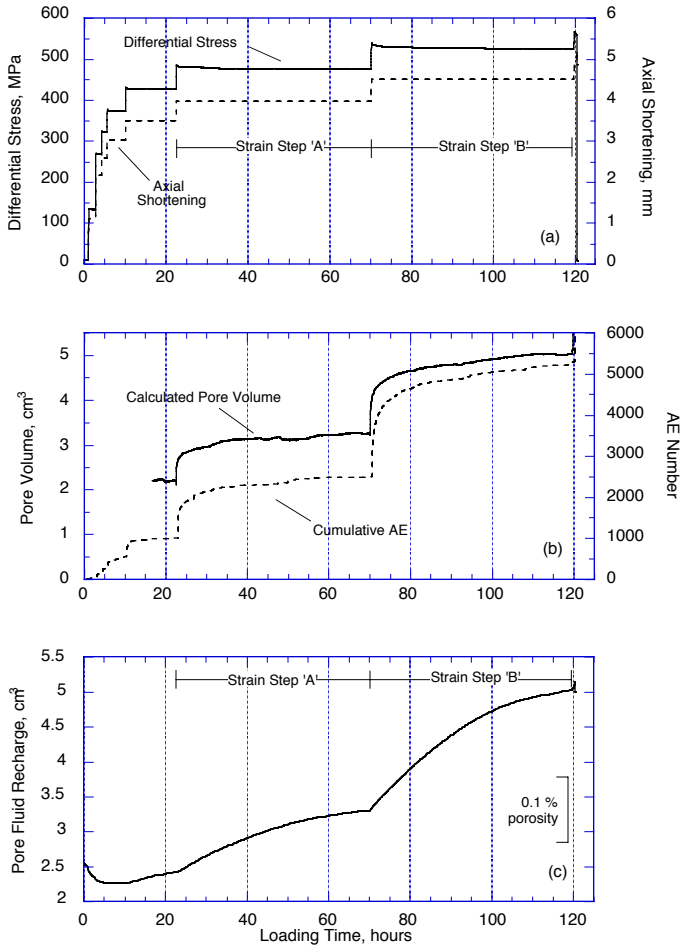

Figure 2. Time history of (a) differential stress ($\sigma_{dif}=\sigma_1-P_c$) and axial shortening during loading sequence, (b) computed pore volume change (arbitrary zero offset) and cumulative number of recorded acoustic emission events, and (c) pore fluid recharge - volume of fluid pumped into sample from external pore pressure system (arbitrary zero offset). Immediately following rapid strain steps, the sample became undersaturated and recharge volume lagged behind true porosity. For the last 10 to 15 hours of strain steps *A* and *B*, pore fluid pressure re-equilibrated and recharge volume represents sample porosity. See Appendix B for analysis.

with a precision of ±0.05 MPa. All displacement and pressure measurements were sampled and recorded at a rate of 1 sample/sec.

Axial shortening was one of the control variables in the experiment and was applied in discrete steps followed by hold periods lasting up to 50 hours. During each hold period time-dependent microcrack growth in the sample would result in a small, gradual drop in axial load as the sample underwent transient creep (Scholz, 1968a, b; Lockner and Byerlee, 1977; Kranz, 1980; Lockner and Byerlee, 1980; Lockner, 1993b) The time history of mechanical loading parameters during the experiment is shown in Figure 2a. Failure occurred at 120.5 hours after initial loading of the sample and approximately one-half hour after the last strain increment was applied. Consequently, little useful velocity information was obtained for this final loading step. During the early loading stages at modest stress levels, time-dependent creep was negligible. The loading steps of greatest interest were

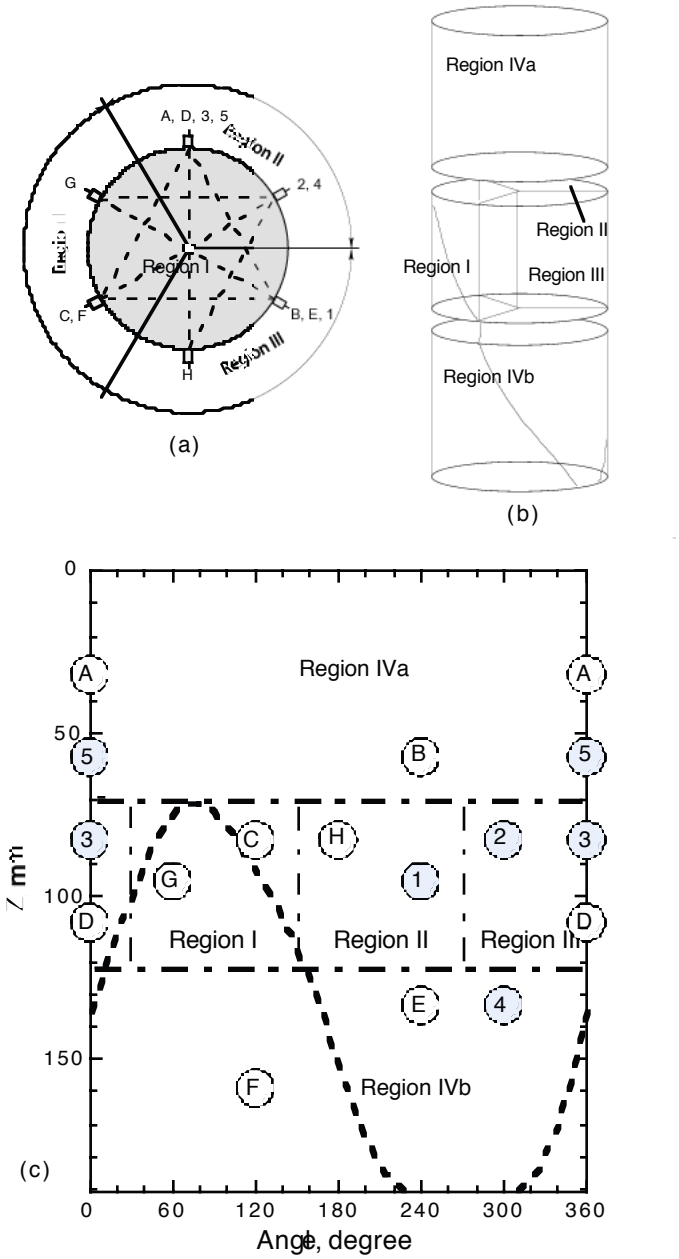

Figure 3. (a) Schematic view along sample axis showing azimuthal position of transducers. (b) Sketch of sample showing Regions I through IV used in velocity and attenuation inversions. (c) Map of transducer positions on sample surface. 1-5 are transmitters; A-H are receivers. Dashed line is the trace of the final fracture surface.

at 480 and 530 MPa differential stress and will be referred to as strain steps '*A*' and '*B*' (see Figure 2a). These occurred at about 86 and 95 percent of peak stress, respectively. Because axial displacement was held constant during these tests, they are best described as stress relaxation experiments.

Fluid volume in the external pore pressure system was recorded continuously during the experiment with a precision of ±0.0005 cm^3. Since the sample and external pore pressure system were a closed system and maintained at constant pore pressure, the recorded pore volume represents the

volume of water flowing into or out of the sample. We refer to this change in pore volume as the sample recharge. Given the sample volume, the recharge, when expressed in terms of volumetric strain, is measured to a precision equivalent to ±0.5 microstrain. The sample recharge history is plotted in Figure 2c. Based on the initial sample volume, one percent porosity is equivalent to 8.69 cm^3, Note that at the beginning of loading, pore fluid recharge rate is negative as water is squeezed out of preexisting cracks. Then, during the later stages of loading at high deviatoric stress, water is continuously pumped into the sample to fill newly formed cracks.

Due to the low sample permeability, the recharge response to a change in sample pore volume has a time constant of many hours. An analytic solution for a 1D recharge model is developed in Appendix A. Calculations of volumetric strain and sample recharge for strain steps *A* and *B* are presented in Appendix B. The slow diffusion time constant implies that pore fluid recharge should deviate significantly from the true pore volume for many hours following each loading increment. To provide direct measurement of volumetric strain, a transversely oriented strain gage was mounted in the sample mid-plane. Unfortunately, this gage failed during initial loading. As a proxy for instantaneous pore volume, we plot a 'calculated pore volume' in Figure 2b. This estimate of pore volume is computed from the axial shortening and recharge volume measurements and is described in Appendix B. Also plotted in Figure 2b is cumulative number of acoustic emission (AE) events recorded during the experiment. The close correspondence between volumetric strain computed from mechanical data and the independent measurement of cumulative AE provides confidence in our volumetric strain calculation. This proportionality between inelastic strain and AE (resulting from microcrack growth) has been reported elsewhere (Yanagidani *et al*., 1985; Lockner *et al*., 1991).

Thirteen piezoelectric transducers (5 transmitters and 8 receivers referred to as 1 to 5 and A to H, respectively) with a frequency range of approximately 200 to 1200 kHz were epoxied to the surface of the rock according to the pattern shown in Figure 3. The arrangement of transducers was chosen to provide dense sampling of the velocity structure in the central region of the sample with special attention to the slow P-wave velocity $V_\perp$ perpendicular to the sample axis (Nur and Simmons, 1969; Lockner *et al*., 1977; Yukutake, 1989). Both transmitter and receiver transducers were 6.35 mm-diameter by 2.54 mm-thick piezoceramic PZT lead-zirconate-titanate transducers. For this size transducer, we can expect a thickness resonance mode of about 800 kHz and a radial resonance mode of about 400 kHz. Also, the preamplifiers used had a lower frequency limit of 120 kHz. As we will show in the Results section, frequency content of the P-wave arrivals appeared to be bimodal with peaks in the 200 to 400 kHz and 800 to 1100 kHz ranges. We interpret the low spectral densities in the 500 to 700 kHz range for all stages of loading as being due to low sensitivity of transducers in this frequency range. Waveforms were recorded on two four-channel digital oscilloscopes with 8 bit amplitude resolution and 0.1 μs sampling rate. Piezoelectric transmitters were excited by a pulse generator with 20V amplitude and 1 μs duration. We developed specialized software for picking the onset of P-wave arrivals which provided an estimated 1% accuracy in determining P-wave velocity.

As seen in Figure 2, deformation steps *A* and *B* each lasted for 48 hours, during which digitized waveform data were collected periodically for the 23 ray paths. From these data, secular changes in P-wave velocity and peak-to-peak amplitudes of P- and S-waves were determined. Since the source and receiver transducers were fixed to the sample and lateral variations in P-wave velocity with time were relatively small, we assume that the ray path and incident angle for each transducer pair did not change during the course of the experiment. Furthermore, since confining pressure, which pressed the transducers to the rock surface, was held constant during the experiment, transducer coupling should also remain nearly constant. Therefore any changes in travel time, amplitude or frequency content during the experiment are due strictly to the propagation characteristics of the rock sample.

P-wave velocity is assumed to be isotropic at the initial hydrostatic loading condition (P_C = 50 MPa and zero deviatoric stress). This is not strictly correct, since Westerly granite has a small inherent velocity anisotropy. However, since we are mainly concerned with changes in velocity, assuming an initial isotropic velocity is not a problem. This assumption allows us to determine travel time corrections (a^i) for each ray path according to

$$\Delta T_0^i = a^i + \frac{D^i}{V_0} \tag{1}$$

where ΔT_0^i is the total travel time for the i-th ray path at hydrostatic pressure, D^i is the length of the i-th ray path and V_0 is velocity at hydrostatic pressure. Then, for later measurements at time t_j, velocity for the i-th ray path is assumed to satisfy

$$V_j^i = \frac{D^i}{\Delta T_j^i - a^i} \ . \tag{2}$$

Due to the large applied deviatoric stress, the sample does change shape during the experiment. At failure, axial and transverse strains are approximately –0.024 and +0.014, leading to gradually increasing systematic errors in the calculated velocities (up to –2.4% for $V_{\|}$ and +1.4% for $V_{\perp}$). These corrections are relatively small compared to the total stress-induced velocity anisotropy that occurs (up to 20%) and have not been applied to the travel time data.

P-wave attenuation of the i-th ray path is given in terms of relative amplitude loss A_p^i per unit distance (expressed in dB/m), according to

$$A_p^i = -\frac{1}{D^i} 20 \log_{10} \frac{Amp_j^i}{Amp_0^i} \ . \tag{3}$$

where Amp_0^i is peak-to-peak amplitude of the first period of the P-wave arrival at hydrostatic pressure and Amp_j^i is peak-to-peak amplitude of the first period of the P-wave arrival for the measurement at time t_j. During loading, the waveform and frequency content of transmitted pulses changed significantly (see frequency content analysis presented in Results section). Therefore, for estimation of attenuation we chose to use the peak-to-peak amplitude of the first period so as to avoid influence of multiply-reflected waves inside the sample.

Experimental Results

Changes in velocity

Results of changing velocity and attenuation for all ray traces are shown in Figures 4 and 5 for the final two strain steps *A* and *B*, respectively. Immediately following each strain step, decreasing velocity and increasing attenuation were observed for all traces. The main difference in the various measurements is in the magnitude of the change. For example, for strain step *B*, trace 2-C, which crosses the central part of the sample (ray path is shown in Figure 3), undergoes a 14% decrease in

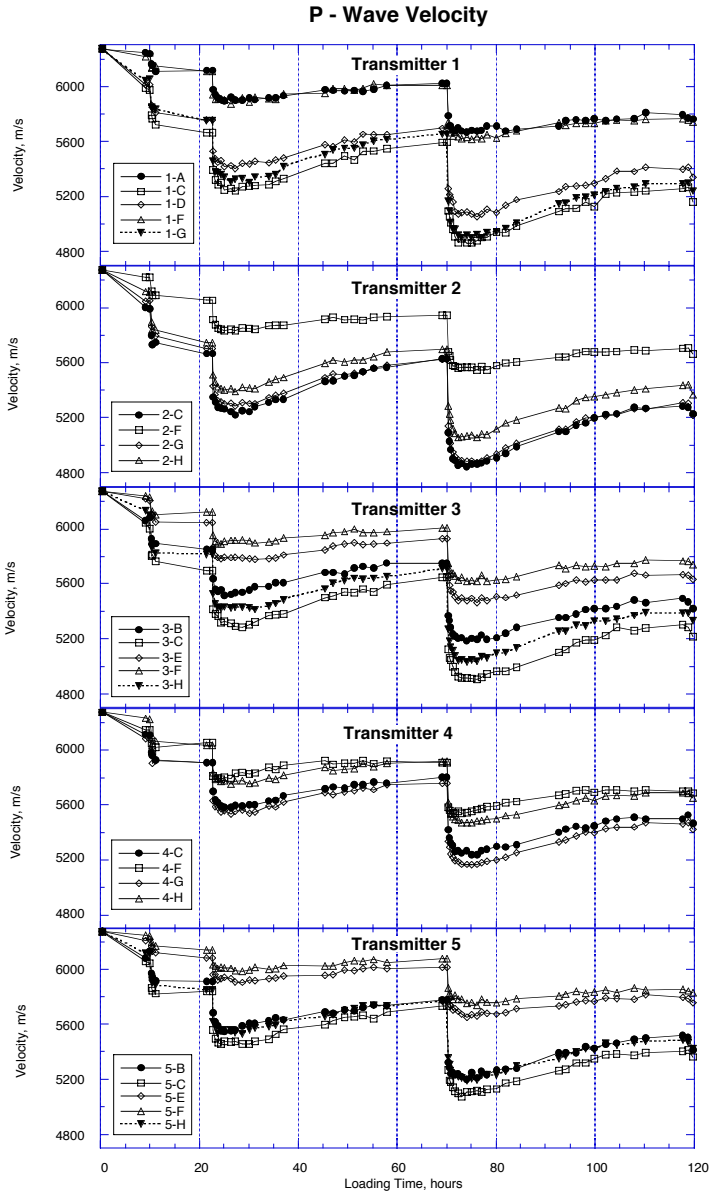

Figure 4. Changes of P-wave velocity along each of 23 ray paths. Strain step *A* begins as 20.5 hrs and strain step *B* begins at 70.0 hrs. Velocities show rapid drop in response to each strain step followed by a recovery beginning 2 to 5 hrs later.

velocity. The corresponding increase in attenuation (*i.e.*, decreases in amplitude) was 11 dB (Figure 5). However, for trace 1-F which traversed the sample at a steeper angle, the decrease in velocity was only 5.5%, accompanied by an increase in attenuation of 3.9 dB. Thus it is clear that a strong anisotropy and spatial heterogeneity developed in both velocity and attenuation during stages A and B. The other general feature observed in all velocity measurements shown in Figure 4 is a delayed recovery in velocity following each strain step. In the next section we argue that the general pattern of sudden drop in velocity followed by a slow recovery is the result of an abrupt opening of microcracks accompanying each strain step, followed by a diffusion-controlled resaturation of these microcracks due to an influx of pore water from the ends of the sample (see Figure 2c).

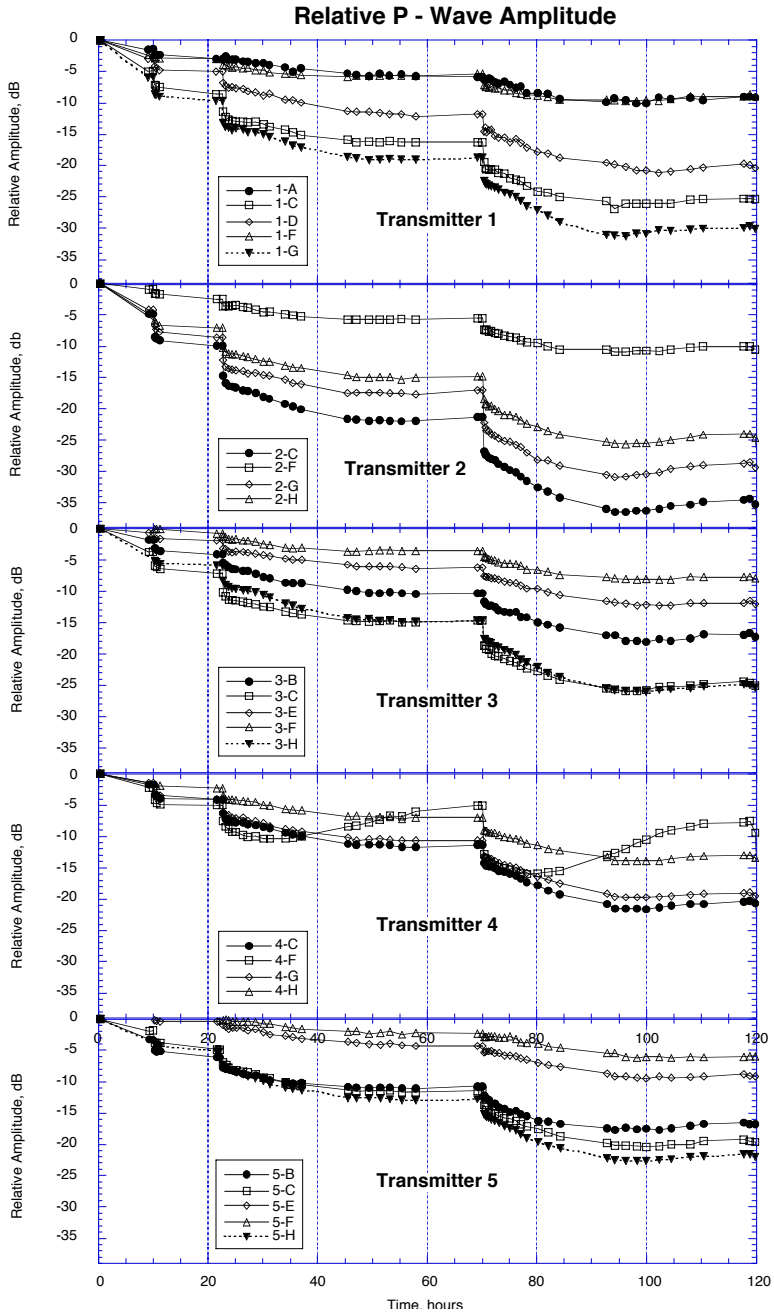

Figure 5. Changes of P-wave amplitude along each of 23 ray paths. Unlike velocity recovery, amplitude recovery begins 20 to 30 hrs after strain steps.

The 23 ray paths represented by the data in Figures 4 and 5 sample propagation parameters in different regions of the sample and along different propagation directions. While these raw data show a number of obvious trends, they do not provide a clear picture of the velocity or attenuation structure within the sample. For example, the apparent grouping of velocities in Figure 4 is simply the result of the limited number of ray paths available and the fact that the declinations of these ray paths happen to fall into two groups. It is therefore desirable to synthesize these observations by fitting them to a simplified velocity model. A detailed tomographic inversion requires many more ray paths

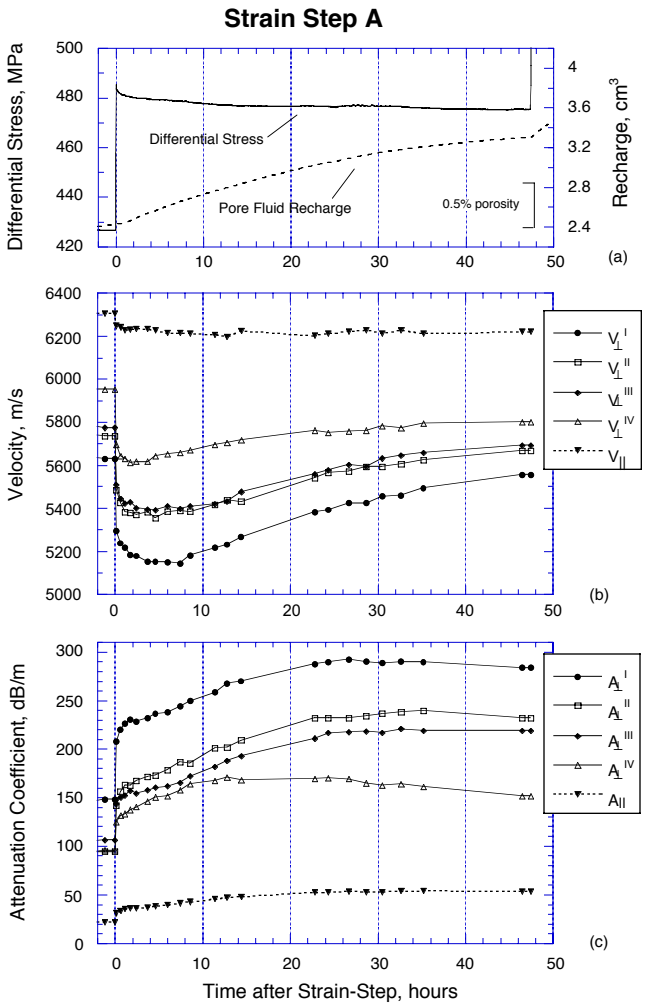

Figure 6. Time histories of strain step *A* (a) differential stress and pore fluid recharge volume, (b) calculated P-wave velocities of 5 element model determined by inversion of data shown in Figure 4, (c) calculated P-wave attenuation of 5 element model determined by inversion of data shown in Figure 5. Region I, showing the lowest transverse velocities and greatest attenuation, was the region that contained the eventual fracture plane and was likely the zone of rupture nucleation. Transverse velocity in Region IV, representing the ends of the sample, was faster than velocities in any of the 3 central regions, indicating less microcrack damage near the ends of the sample (see text). Velocity recovery began near the ends of the sample (Region IV) after approximately 2 hrs but was delayed in the central region until 3 to 5 hrs after the applied strain step. Attenuation recovery occurred first near the sample ends after 10 to 14 hrs and in the central region after 25 to 30 hrs.

than are available in this experiment. To assure robustness of the inversion and to avoid non-uniqueness problems, we have solved for a five element velocity model. Additional modeling involving additional velocity elements may be carried out in the future. Due to the axial symmetry of the applied stress field and resulting microcrack damage, we assumed an axi-symmetric velocity field similar to earlier analyses (Bonner, 1974; Lockner *et al.*, 1977; Yanagidani *et al.*, 1985; Lockner *et al.*, 1992a; Lockner, 1993a). Thus, locally, velocity is assumed to obey an elliptical law described by

$$V^{i2} = V_{\perp}^2 \sin^2 \phi^i + V_{\parallel}^2 \cos^2 \phi^i \qquad (4)$$

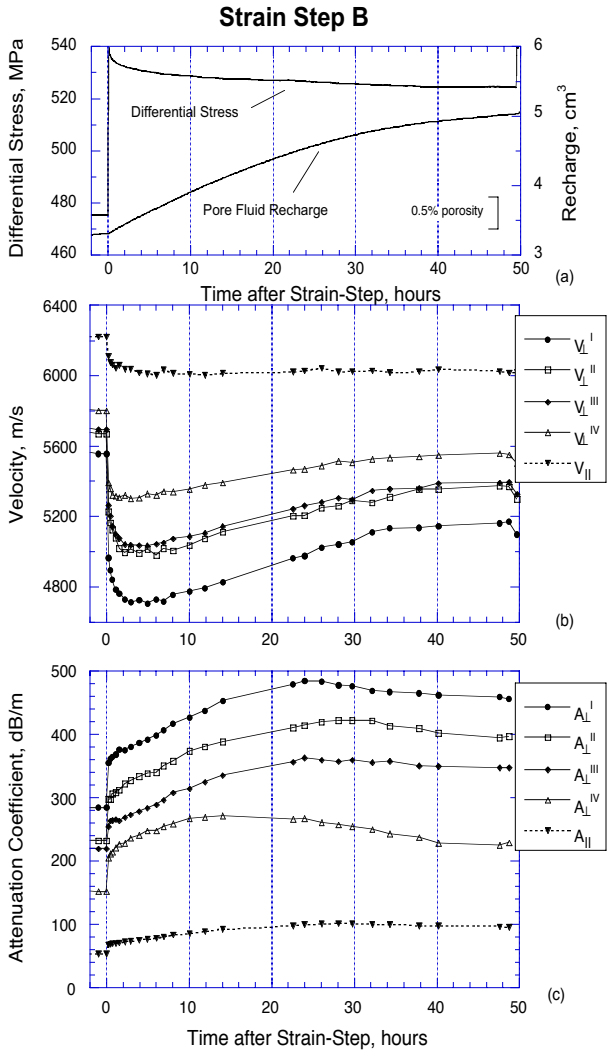

Figure 7. Time histories of strain step B (a) mechanical parameters, (b) calculated P-wave velocities of 5 element model, (c) calculated P-wave attenuation of 5 element model. Timing of the velocity and attenuation response was much like the response to strain step *A*.

where $V_{||}$ and $V_{\perp}$ are velocities parallel and perpendicular to the sample axis (maximum compressive principal stress direction), respectively, and ϕ^i is the angle that the i-th ray path makes with respect to the sample axis. Equation (4) actually defines an ellipse for the P-wave slowness (reciprocal of velocity). When inverting velocity data, we find that this form of the angular dependence of velocity provides a better fit than the form in which the velocity itself has elliptical dependence on propagation direction. Equation (4) is the form adopted by Yanagidani *et al*. (1985).

P-wave velocities, determined at each measurement time t_j, were inverted to fit a three-layer symmetrical model in which the central layer with thickness of 50 mm, was subdivided into three equal wedge-shaped regions, referred to as I, II and III (see Figure 3). The orientation of these regions was chosen so that the eventual fracture plane was restricted to Region I. The transducer array was designed so that most ray paths crossed the central portion of the sample. In addition, placement

of transducers on the sides and not the ends of the sample meant that velocities perpendicular to the sample axis could be measured directly, but axial velocity must be inferred since there were no ray paths parallel to the sample axis. Thus, raw data provide a better constraint on $V_\perp$ than on $V_\parallel$. Also, as already mentioned, there is better ray path coverage of the central region of the sample than of the sample ends. Consequently, two additional simplifying assumptions were made in the layered model. First, the two end regions of the sample were assumed to have the same velocity, referred to jointly as Region IV. Second, all regions were assumed to have the same axial velocity ($V_\parallel$). Using these assumptions, the P-wave velocity inversion solved for five independent parameters: ($V_\parallel$, $V_\perp^{\mathrm{I}}$, $V_\perp^{\mathrm{II}}$, $V_\perp^{\mathrm{III}}$, and $V_\perp^{\mathrm{IV}}$). With data from only 23 ray paths, this proved to be the maximum number of parameters that could be reliably determined. It is reasonable to expect that most microcracking and dilatancy tend to occur in the central region since the ends of the sample are prevented from expanding laterally due to frictional contact with the more rigid steel endcaps. This is why we chose to concentrate the transducer array near the center of the sample. Furthermore, fault nucleation studies (Lockner *et al.*, 1992a) show that faulting in this test configuration is likely to originate in the central region of the sample. Time histories of the P-wave velocity inversion parameters are plotted in Figures 6b and 7b. The largest changes in $V_\perp$ do in fact occur in the central part of the sample. A maximum velocity anisotropy of 22% developed in Region I at the beginning of strain step B (Figure 7b).

Changes in attenuation

Figure 5 shows that in addition to velocity, the P-wave attenuation in the sample became anisotropic and inhomogeneous during the experiment. Amplitude of trace 4-F appeared anomalously sensitive to strain steps even though the velocity did not seem unusual. Amplitude of this trace recovered to values more consistent with the other transducers after about 30 hours. We have no explanation for this unusual amplitude response. Amplitudes of other traces showed an initial decrease and then stabilized or even increased after 20 to 30 hours. To approximate the overall attenuation structure, we fit the data shown in Figure 5 to the same model used for the velocity structure. Once again, we assumed that attenuation had axial symmetry and in each region the P-wave attenuation obeyed

$$\frac{1}{A^{i2}} = \frac{\sin^2 \varphi^i}{A_\perp^2} + \frac{\cos^2 \varphi^i}{A_\parallel^2} \tag{5}$$

where A^i is the attenuation in the direction defined by declination φ^i; and $A_\parallel$ and $A_\perp$ are attenuation parallel and perpendicular to the sample axis, respectively. Results for strain steps A and B are shown in Figures 6c and 7c. Both axial velocity and attenuation showed little sensitivity to the accumulation of microcrack damage while transverse components were strongly dependent on the accumulation and growth of microcracks. This experimental observation can be explained by opening of microcracks, oriented sub-parallel to the sample axis (Tapponnier and Brace, 1976), which provide greater dilatation and compliance in transverse directions.

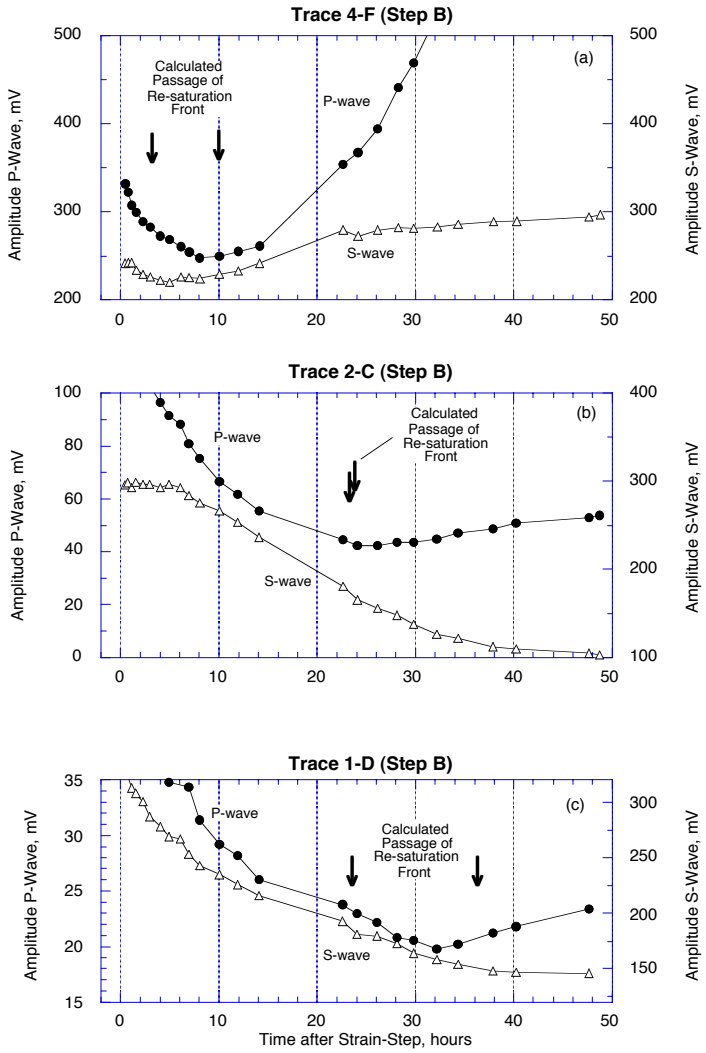

Figure 8. P-wave and S-wave amplitude history of selected traces. Trace 4-F is near the bottom of the sample while 2-C and 1-D are near the sample mid-plane and fracture nucleation zone. Vertical arrows indicate the beginning and ending of passage of the resaturation front past each trace as modeled by the 1D flow model described in Appendix B. Since shear wave attenuation is much less sensitive to partial saturation than compressional wave attenuation, we expect the onset of the P-wave amplitude recovery to correspond to the passage of the resaturation front.

Soon after application of each strain step, the transverse components of velocity dropped, accompanied by a simultaneous increase in attenuation. It is worth noting that the eventual fault nucleation zone (Sector I) had the lowest velocity and greatest attenuation in the sample during both strain steps *A* and *B*. Following both strain steps, P-wave velocity first decreased steadily, and then, after a few hours, reversed and slowly recovered (Figures 6b and 7b). Near the ends of the sample, the velocity minimum occurred approximately one hour after the strain steps. In the central sectors, the minimum occurred 1.5 to 3 hours after the strain steps.

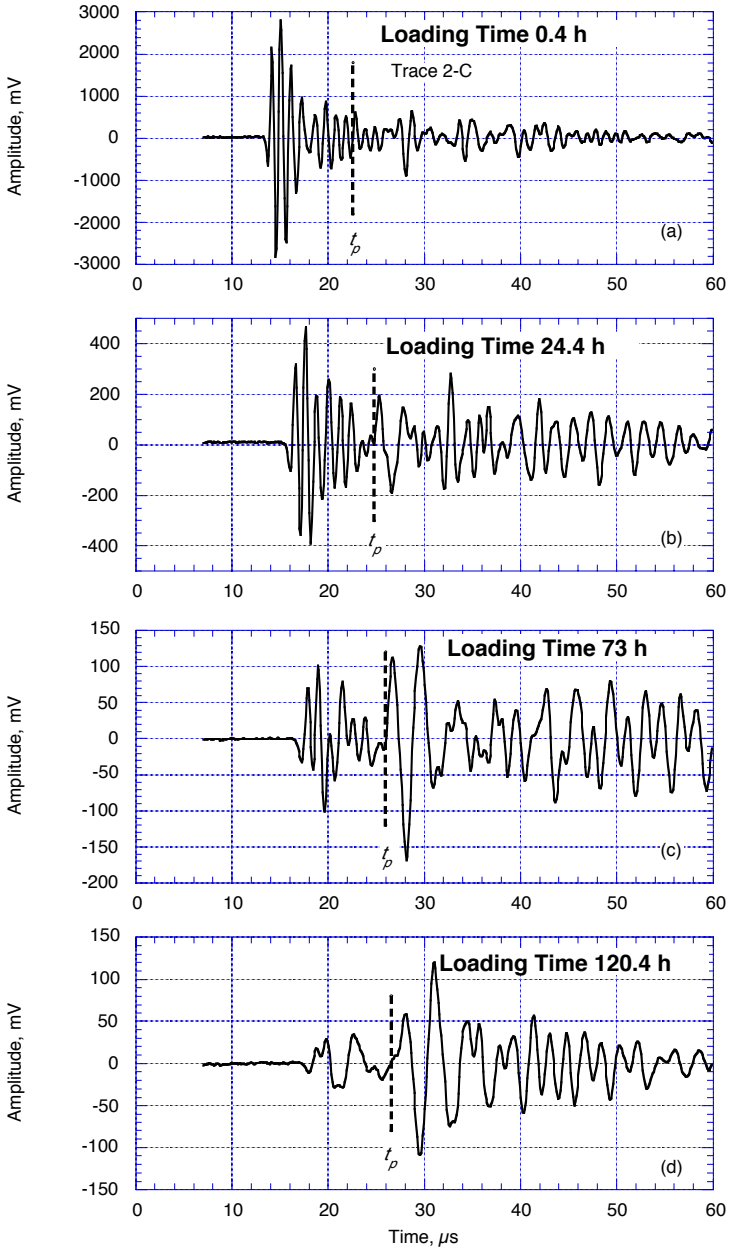

Figure 9. Waveforms recorded for trace 2-C at different loading times (see loading history in Figure 2). End of the P-wave packet used to evaluate frequency content is indicate by t_p.

Ten to 30 hours after application of the strain step, the change of attenuation reversed sign (i.e. amplitude started to increase). The timing of the attenuation rate reversal was different in different parts of the sample. Regions near the ends of the sample showed the reversal earlier than regions near the center (see Figure 5). For example, attenuation near the ends of the sample ($A_{\perp}^{IV}$ in Figures 6 and 7) begins to decrease 14 hours after application of the strain-step, while the center of the sample ($A_{\perp}^{I}$, $A_{\perp}^{II}$ and $A_{\perp}^{III}$) took nearly twice as long to show a reversal.

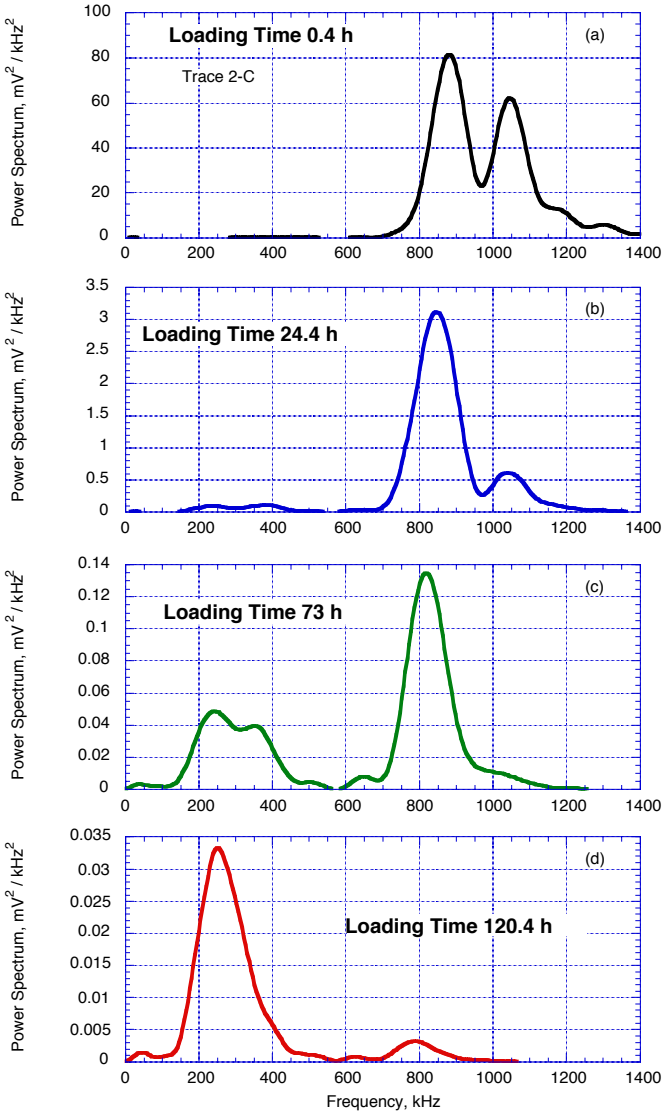

Figure 10. FFT power frequency spectrums of longitudinal waves shown in Figure 9. Bimodal response indicates dominant response modes of the transducers. Progressive loss of high frequency occurs as microcrack damage accumulates in the sample.

As shown in Figure 2, pore volume steadily increased during all stages of loading, implying the continual appearance of new sources of elastic energy absorption. Therefore, decreasing attenuation is apparently associated with the filling of the opened cracks by the water. This conclusion is also supported by analysis of longitudinal and shear waves. The results for selected traces are presented in Figure 8 showing that the amplitudes of P-waves reached a minimum and then started to recover at different times, while the amplitudes of S-waves continued to decrease. The times when water first reached individual ray paths and then completely filled them, as deduced from the calculations presented in Appendix B, are shown by the arrows in Figure 8. There is good agreement between the

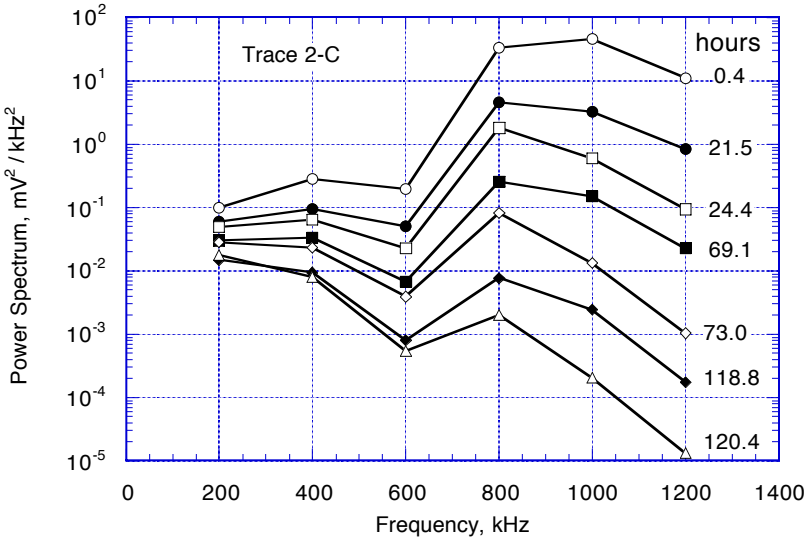

Figure 11. FFT power spectrum data shown in Figure 10 but averaged over 200 kHz intervals.

calculated position of the water front and the direct measurements of the parameters of ultrasonic waves.

Spectral analysis of waveforms

The waveforms recorded for trace 2-C, crossing the sample center (see transducer positions in Figure 3) are presented in Figure 9. The waveform recorded before application of axial load (only confining pressure was applied) is shown in Figure 9a. Waveforms recorded soon after applying the last three strain steps are shown in Figures 9b-9d. A significant change in the character of the waveforms can be seen. Peak-to-peak amplitudes of longitudinal waves are 5626, 860, 103 and 63 mV for Figure 9 a, b, c and d, respectively indicating that amplitude decreased by about a factor of 90 during loading. The times t_p of the ends of the P-wave selections used in our analyses are shown in Figure 9 as vertical dashed lines. Frequency spectra of the selected longitudinal waves are presented in Figure 10, showing that the progressive increase in attenuation is frequency dependent, i.e. the higher frequencies are most attenuated. Note the successive increase in vertical scale of the four plots.

The bimodal nature of the response spectrum of the ultrasonic transducers used for the velocity/attenuation measurements has been noted in the Experimental Procedure section. The transducers are most sensitive to excitation of radial and thickness modes with frequencies of about 400 and 800 kHz. We interpret the low spectral densities in the range 500 to 700 kHz for all stages of loading as being due to low sensitivity of transducers in this frequency range. We apply an approximate correction for this frequency-dependent transducer response in the following way. First, all spectral density data were averaged using 200 kHz intervals. These averaged spectral densities are plotted in Figure 11 for different stages of loading. Next, we normalized the spectral densities using the values measured before differential stress was applied to the sample (Figure 10a, at P_c = 50 MPa). Results are shown in Figure 12. Since the transducers were undisturbed during the experiment, any changes in the waveforms must result from changes in the wave propagation properties of the sample due to microcrack growth and variations in pore fluid content. Therefore, Figure 12 shows the relative change in spectral density (relative P-wave attenuation) during the different stages of loading. Because we used the Fast Fourier Transform (FFT) of the Power Spectrum, the values on Figure 12 correspond to the attenuation of energy (twice the value of amplitude attenuation). The highest

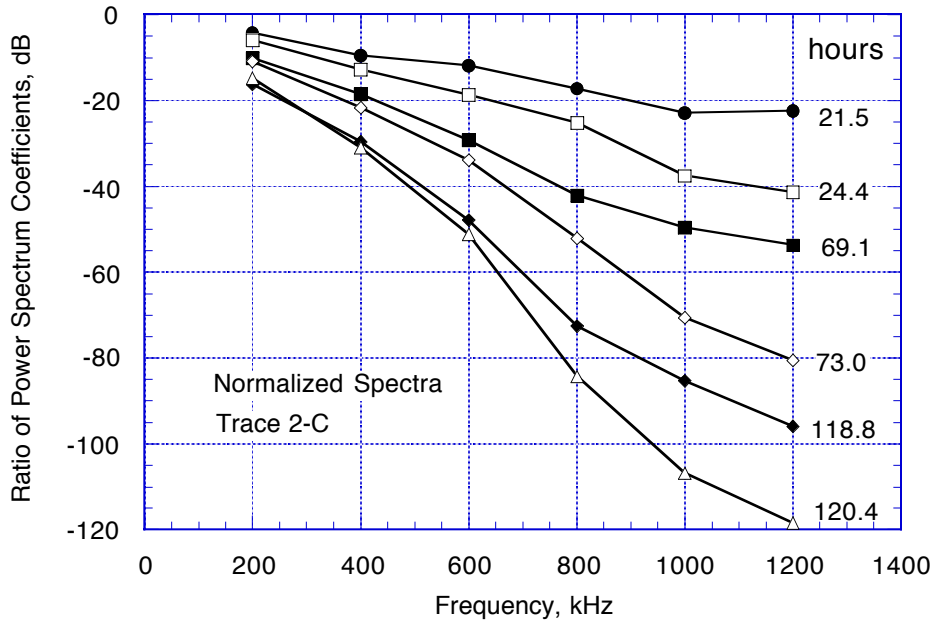

Figure 12. FFT power spectra normalized by the power spectrum of the zero deviatoric stress record.

frequencies have the highest attenuation: for example in the frequency range 100 to 300 kHz attenuation increased by 16 dB, while for the highest measured frequencies of 1100 to 1300 kHz, attenuation increased by 118 dB.

Relative attenuation is shown in Figure 12 at discrete times. The continuous time variation is shown in Figure 13 by plotting relative attenuation as a function of time and frequency. The applications of strain steps *A* and *B* are indicated by the dashed lines. Rapid increases in attenuation occur at all frequencies in response to the sudden strain (stress) steps, although the higher frequencies were affected more. Then, a few hours after the strain steps, change in attenuation decreased to a slower, but steady rate. This change in attenuation in response to a sudden strain step is similar to the accumulation of microcracks in the sample, as we discuss in Appendix B.

Discussion

The velocity/attenuation response of the granite sample to a rapid strain step at high differential stress showed a complex evolution. The analysis that we present indicates that rapid dilatant microcrack growth in response to the stress steps in intervals *A* and *B* was sufficient to reduce the initial 1 MPa pore pressure within the sample to less than vapor pressure, causing the pore space to become undersaturated. This sudden loss of liquid phase within the pores resulted in an abrupt drop in P-wave velocity and increase in attenuation. P-wave velocity began increasing one to six hours later. Our calculations suggest that this was too soon to coincide with sample resaturation and instead may be the result of local redistribution of water within the pores. Resaturation of the pore space then progressed over a matter of many hours as water diffused into the sample from both ends. With passage of the resaturation front, P-wave velocity continued to recover and attenuation either stabilized or began to decrease. In the remainder of this paper we present evidence to support this model and to explore implications that it has for natural observations.

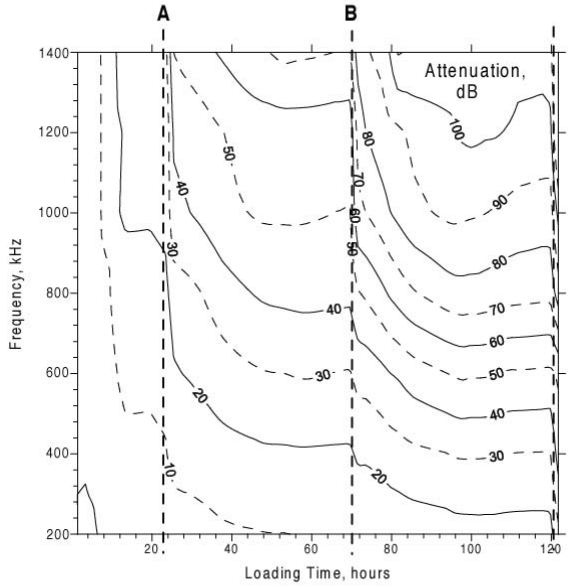

Figure 13. Relative attenuation as a function of time and frequency using all 55 waveforms recorded for trace 2-C during the experiment. Application of strain (loading) increments are indicated by times A and B. Strain steps produce an immediate increase in attenuation followed by a continued increasing attenuation for 20 to 30 hrs. Then, high frequencies show a reversal or reduction in attenuation while low frequencies produce nearly constant attenuation.

Computed velocity and attenuation fields following stress steps

Both velocity and attenuation measurements show that after application of the strain step the sample becomes anisotropic (Figures 6 and 7). It is well known that new microcrack damage tends to be aligned sub-parallel to the maximum compressive stress direction (parallel to the sample axis) (Tapponnier and Brace, 1976; Lockner *et al*., 1992b; Moore and Lockner, 1995). This alignment of microcracks corresponds to the anisotropy reported by Mavko *et al*. (1995), in which they too observed faster velocity and lower attenuation in the axial direction. They explained these results in terms of closing of cracks that are nearly perpendicular to the axis of compression. The tendency for cracks parallel to the sample axis to open while cracks perpendicular to the axis are closed implies that $V_{\perp}$ and $A_{\perp}$ should show larger changes than $V_{\parallel}$ and $A_{\parallel}$. Consequently, $V_{\perp}$ and $A_{\perp}$ are the most important to study in terms of likelihood of detectable field observations.

This study also shows that with the application of deviatoric stress the sample becomes heterogeneous. The P-wave velocity inversion shows that the central portion of the sample has

significantly lower transverse velocity than the ends, as expected from the lateral restraining effects of the rigid steel endcaps (see discussion above). These results are in good agreement with previous experiments (Lockner and Byerlee, 1977; Masuda *et al*., 1990; Lockner *et al*., 1992a) which showed that fault nucleation consistently occurred in the central region of samples under these triaxial test conditions.

The decrease and subsequent recovery of P-wave velocity occur first in the confined ends of the sample, then in the central zone. In addition, the central layer itself becomes more heterogeneous immediately after each loading step. The drop of transverse velocity in Region I is more than in Regions II and III, and is accompanied by higher attenuation. Similar findings were reported for P-wave velocity inversions of dry granite samples by Yukutake (1989; 1992) The macroscopic fracture that eventually formed, and was responsible for sample failure, crossed through Region I. (The trace of the fracture intersecting the sample surface is shown in Figure 3). Consistent with previous experiments (Lockner and Byerlee, 1980; Masuda *et al*., 1990; Lockner *et al*., 1992a) the eventual rupture plane apparently nucleated in Region I. In the earlier investigations carried out on dry samples (Lockner *et al*., 1977; Moore and Lockner, 1995), it has been shown that a decrease of velocity and increase of attenuation are connected with opening cracks tending to be aligned sub-parallel to the sample axis. Apparently, Region I was the weakest part of the sample, and the process of new crack growth was more active here. As a result, acoustic properties of this zone became anomalous even at loading interval *A* representing 86% of peak stress. The analysis in Appendix B suggests that the sample became fully saturated 36 hours after application of the strain step. Later, additional pore fluid was required only for filling newly forming and dilating cracks. According to this analysis, the newly created porosity along different ray paths would become saturated with water at different times. The timing of resaturation is consistent with the changes of P-wave and S-wave amplitude measurements (Figure 8). This P and S amplitude response is similar to findings of Cadoret *et al*. (1995) who showed that water content has a strong influence on compressional wave attenuation but has little or no influence on torsional attenuation. Thus we infer that the P-wave amplitude for a particular ray path starts to increase, or at least stabilize, when full saturation of that ray path has been reached. The fact that P-wave velocity generally recovers before attenuation (Figures 6 and 7) implies that different mechanisms are controlling these parameters.

The main attenuation mechanisms in this experiment are apparent attenuation, or elastic scattering, and intrinsic or frictional and viscoelastic attenuation. The mechanisms for apparent and intrinsic attenuation are different. In apparent attenuation acoustic energy is redistributed to the later portions of the wave field while in intrinsic attenuation the energy is actually removed from the wave field and dissipated as heat. However both mechanisms cause reduction in amplitude of the initial part of the recorded signal. Most of the scattering mechanisms (for example random-phase scattering) become important only when the wavelength of the elastic wave is close to the size of the heterogeneities (Blair, 1990; Mavko *et al*., 1998). The frequency range of our source transducers was 200 to 1200 kHz. Therefore the shortest wavelength (corresponding to the highest frequency) should be about 4 mm. This wavelength is much longer than the size of the microcracks in the rock, which are generally limited by the grain size (~0.2 mm). Therefore it is unlikely that we would observe significant elastic scattering from individual microcracks. The increase in microcrack density in Westerly granite has been documented in thin section studies (Hadley, 1976; Madden, 1983; Lockner *et al*., 1992b; Moore and Lockner, 1995). The accumulated microcrack damage induced by high deviatoric stress is dominated by microcracks smaller than about 100 microns. However, Blair (1990) showed that scattering due to grain clusters rather than individual grains is a dominant attenuation mechanism for dry granite. In the case of an elastic wave passing through a cluster of fractures, the effect of

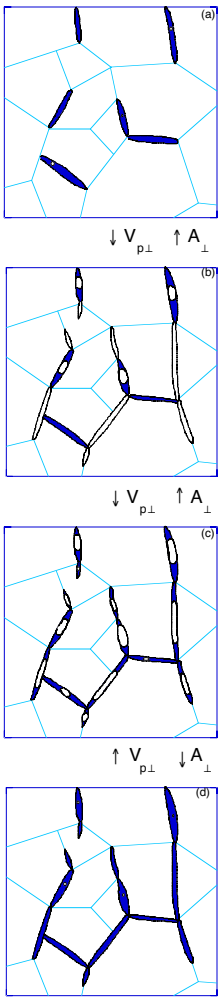

Figure 14. Idealized sequence of crack growth and resaturation corresponding to times indicated in Figure 8. Shaded cracks are liquid-filled; unshaded portions of cracks are vapor-filled (a) Pre-existing cracks are fully saturated. (b) Following stress step, new (dry) cracks open and favorably oriented existing cracks open and become partially saturated. (c) Before recharge from external pore fluid system can resaturate cracks, local redistribution of pore water occurs to wet crack surfaces and minimize vapor-bubble surface area. With time, this process tends to eliminate small bubbles and leads to partial recovery of P-wave velocity. (d) Eventually, diffusion of water from outside the dilatant zone results in resaturation of all pores, recovery of pore fluid pressure, a further increase in P-wave velocity and partial decrease in P-wave attenuation due to reduced efficiency of squirt-flow loss mechanism.

scattering may be significant. At low frequencies, for which the wavelength is larger than the size of the scatterers, the apparent attenuation has a strong frequency dependence: $\sim f^n$, where f is frequency and n varies for different models of scattering in the range from 1 to 4 (Menke *et al.*, 1984; Dubendorf and Menke, 1986). Therefore, one of the possible mechanisms of the observed frequency-dependent attenuation in our experiments (Figures 10-13) can be apparent attenuation. Other models describing the energy loss in saturated rocks are Biot's model of poroelastic attenuation (Biot, 1956) and the squirt-flow mechanism of viscoelastic attenuation (Mavko and Nur, 1979). Both of these mechanisms are likely to be contributing to the changes in attenuation that we have observed.

Fluid undersaturation/recharge model

One interesting result of this investigation is the large drop and then recovery to 98 and 94% of the original value of P-wave velocity for strain steps *A* and *B* respectively. We attribute the initial drop in velocity to opening of unsaturated microcracks within the rock. The beginning of the velocity recovery appears in the central region approximately 6 hours after application of the strain-step. This delay is too short to be explained by the simple recharge model presented in the Appendix, which is in good agreement with the results of the amplitude recovery analysis (Figure 8). We propose that the recovery in P-wave velocity is the result of local redistribution of water within the pore space in response to the sudden appearance of new microcracks. According to the estimates shown in Appendix B, the values of volumetric strain which appeared at strain steps *A* and *B*, should be about $\phi \approx 0.64 \times 10^{-3}$ and $\phi \approx 1.35 \times 10^{-3}$, respectively. Taking into account compressibility of water, $C_w \approx 4 \times 10^{-4}$ MPa^{-1}, we conclude that coincident with strain steps *A* and *B*, pore fluid pressure dropped below the vapor pressure of water and the sample abruptly changed from full saturation to partial saturation (Figure 14b). In this case the pre-existing pores contained wetted surfaces surrounding bubbles of water vapor. Opening of new (dry) cracks, which were connected with these pre-existing partially saturated cracks would result in diffusion of water molecules into the new void space driven by pressure gradient and surface tension effects (Figure 14b to 14c). This process would stop after reaching a new equilibrium distribution of liquid and vapor in the pore space. The newly formed cracks in granite are very thin (low aspect ratio) and it is energetically favorable to have their surfaces, and especially narrow crack tip regions, wetted with liquid water, leaving the vapor phase in the more open void spaces. The size of these cracks will be comparable to or smaller than the grain size (~ 0.2 mm) (Moore and Lockner, 1995). For coexistence of water liquid and vapor at room temperature, the vapor pressure must be low (approximately 3 kPa). Thus, following the strain step, the process of the local redistribution of water from pores to new cracks will begin. The redistribution of vapor bubbles from long, thin shapes to near-spherical shapes as the pore fluid re-equilibrates, results in a wetted pore structure that appears stiffer to compressional wave motion and results in increased P-wave velocity. This process should contribute to the recovery of P-wave velocity while attenuation was still increasing. As mentioned earlier, the lateral strain is greater in the central part of the sample than near the ends, which are prevented from expanding by frictional contact with the steel end pieces. Therefore, we expect that crack density is greater in the center of the sample than near the ends and the process of redistribution of water from pores to newly-formed thin cracks will be completed more quickly in the end regions than in the center (see Figures 6 and 7).

In addition to the readjustment of pore fluid, each stress step should be followed by an extended period of primary or transient creep (Scholz, 1968b; Lockner and Byerlee, 1977; Lockner, 1993b, 1998). This is a period in which inelastic strain rate (microcrack growth) and acoustic emission decay as 1/t. The accumulation of new microcrack damage during this interval will lead to a further decrease in $V_\perp$ and increase in $A_\perp$. At high deviatoric stress, transient creep progresses into a prolonged period of secondary creep (see, for example, (Lockner and Byerlee, 1980)) characterized by steady microcrack growth. The nearly constant recharge rate during the final hours of both strain steps *A* and *B* (Figure 2c) suggests a transition to secondary creep.

Following the rapid transient creep and local readjustment of pore fluid (1 to 4 hours in Figures 6 and 7), a protracted period of partial saturation existed in the sample as recharge water flowed from the external pore fluid system. Complete resaturation near the ends of the sample required approximately 10 hours and more than 30 hours in the central region (as inferred by the numerical

modeling and the velocity and attenuation transients). This transitional period of partial saturation exhibited the unusual characteristic of increase of both $V_\perp$ and $A_\perp$ (Figures 6 and 7). We suggest two processes that contribute to this effect. First, a gradual influx of water ahead of the full saturation front would shrink vapor phase bubbles. Second, a steady loss of small bubbles and concentration of vapor phase into fewer large bubbles would be driven by surface tension effects. Both processes would contribute to recovery of P-wave velocity (although a change in the population of bubble sizes might be measurable in terms of velocity dispersion characteristics). Also, since the viscous drag of the vapor phase is small, a gradual increase in the amount of liquid phase water would increase viscous attenuation through both the Biot mechanism and the squirt-flow mechanism (discussed, for example, by Dvorkin and Nur (1993)). According to this model, when an elastic wave propagates through a partially saturated rock (for example having residual gas in pores) the fluid will flow not only parallel (Biot's flow), but also perpendicular (squirt flow) to the direction of propagation due to the dynamic deformation of the rock. This flow causes viscous losses and therefore attenuation of the elastic wave. Mavko and Nur (1975) suggested that squirt flow may occur even in fully saturated rocks due to fluid flowing between saturated cracks of different orientation. However we expect these loss mechanisms will have different magnitudes depending on the degree of saturation. The change in slope of the attenuation curves (Figure 8) associated with passage of the saturation front can be explained as the result of a change in mechanism from a partially to fully saturated condition. We believe that P-wave attenuation begins to decrease only after water has filled all pores and cracks whose sizes are comparable with the test wavelength; i.e., after full saturation of the pores along a given ray path. The timing of this process depends on the position of the individual trace (see Figure 8). Therefore we suggest that P-wave velocity is more sensitive to the process of redistribution of internal water, while the P-wave amplitude is more sensitive to the process of full resaturation of the rock.

In the preceding discussion we propose the occurrence of numerous attenuation mechanisms which operate on different time scales within the sample. For clarity, we summarizing this sequence: 1) Microcrack density increases immediately in response to each applied stress increment. This is followed by additional microcrack growth with a 1/t decay in growth rate (transient creep) lasting for a period of hours and gradually evolving to secondary creep reflecting constant microcrack growth. These processes reflect the accumulation of irreversible microcrack damage and are observed in both wet and room dry samples. They result in decreasing P and S-wave velocity and increasing attenuation due to scattering and intrinsic loss mechanisms. 2) The rapid stress increase causes dilatancy, reduced pore pressure and appearance of a water vapor phase (Figure 14b). The coexistence of two pore fluid phases leads to enhanced attenuation through Biot and squirt-flow mechanisms. 3) Local readjustment of vapor phase driven by surface tension effects (Figure 14c) leads to compressional velocity recovery but has little effect on Biot and squirt-flow attenuation mechanisms. 4) Resaturation of pore space leads to pore pressure recovery as well as continued recovery of compressional wave velocity (Figure 14d). Loss of vapor phase reduces the effectiveness of the squirt-flow mechanism and attenuation either stabilizes or recovers.

Application to earthquake nucleation zone

As we mentioned earlier, the nucleation zones of moderate earthquakes may be less than 100 m across. If a seismometer were placed 10 km from such a nucleation zone in which seismic velocities changed by 50%, we would observe only a 0.5% change in total travel time (or in average seismic velocity values). Even using modern techniques it would be difficult to identify such small changes in velocity. However, using high quality down-hole seismometers, it may be possible in a well-controlled

experiment to record such changes. It may in fact be possible to carry out field measurements that provide supporting evidence for the Dilatancy-Diffusion model. It is possible that during the long period of earthquake preparation, regions larger than 100 m which would represent an individual nucleation site, may be involved in dilatant deformation. Certainly the earth's crust is heterogeneous so that tectonic loading could produce clusters of dilatational regions. Then, during water saturation of these regions we might expect measurable changes in travel time. Furthermore, we have found that in the laboratory, attenuation of elastic waves and especially frequency-dependent attenuation is much more sensitive to the process of dilatancy than is wave velocity. We have measured high frequency attenuation of power density of as much as 118 dB in response to a 70 MPa stress step. Consequently, the high frequency component of the transmitted wave decreased in amplitude by a factor of almost 1000. If similar effects occur in the earth, then combining velocity structure and attenuation data may provide useful information regarding time-dependent changes in earthquake source regions. The attenuation mechanisms observed in this study are operative in the 100 to 1200 kHz range and are associated with processes occurring on the grain scale. Scaling laws must be applied to determine the attenuation mechanisms that would be operative at the lower frequencies appropriate to field measurements. Scattering by fracture networks and damage zones associated with active faults is not unreasonable to observe. Reduced velocities associated with active fault zones have also been observed using 2D and 3D seismic imaging.

Measurement of coseismic and post seismic changes in velocity and attenuation may provide a more easily observable signal than the changes expected to result from a developing nucleation zone. Advantages over measurement of precursory transients include the fact that coseismic changes are likely to involve larger portions of the fault and involve more rapid and larger stress transients. Coseismic development of a vapor phase through frictional heating has long been recognized as a possibility for large magnitude earthquakes (Sibson, 1973; Lachenbruch, 1980; Lockner *et al*., 1983; Andrews, 2003) A velocity/attenuation transient of the type reported here might be observable for a short period following a large earthquake as pore fluids and pore fluid pressure re-equilibrate within the fault zone. Recent reports of the recovery of fault zone trapped wave velocities following large earthquakes (Li and Vidale, 2001) may also be observing processes similar to those reported here for laboratory samples. Trapped wave studies may eventually provide a means of detecting precursory changes associated with earthquake nucleation zones that are beyond our current capabilities.

Conclusions

We have shown that following incremental loading of an intact granite sample, velocity and attenuation of transverse P-waves are sensitive to the formation of microcracks and to the saturation of these cracks as water flows from the surrounding regions. Preferred orientation of newly formed microcracks leads to anisotropic velocity and attenuation fields which evolve in a systematic and complex manner in response to changes in stress, strain and influx of water. The complex relation between resaturation, time-dependent crack growth and high frequency attenuation indicates significant contributions of scattering, Biot and squirt-flow attenuation mechanisms. The immediate response to a stress step is a sudden drop in transverse P-wave velocity and increase in attenuation. Resaturation of the sample leads to partial recovery of P-wave velocity while attenuation continues to increase. The eventual fracture plane apparently nucleates in the low-velocity/high attenuation zone (Region I) which could be distinguished by 86% of peak stress. Application of deviatoric stress steps resulted in rapid dilatation and undersaturation of the sample, implying a sudden drop in pore

pressure from 1 MPa to nearly zero. This pore pressure drop results in dilatancy hardening which is gradually negated as recharge water diffuses into the sample.

Appendix A: Resaturation Model

We analyze the flow of water into the sample following strain steps *A* and *B* (show in Figures 6a and 7a). During the experiment a constant pore pressure p = 1.0 MPa was maintained at the two ends of the sample. 'Pore Fluid Recharge' as labeled in those plots is the amount of water that flows into the sample. A strain gauge attached to the sample to measure radial strain malfunctioned at the beginning of the experiment so that any inferences about the timing and magnitude of volumetric strain changes must come from the pore fluid volume observations. Previous experiments on Westerly granite have shown that the total porosity at the start of the experiment was approximately 0.1%. Care was taken to pre-saturate the sample before the start of the experiment, providing an approximate reference point for the pore fluid volume curve (Figure 2c). Over the course of the experiment, porosity increased by approximately 0.3%. The imposed axial strain steps at the beginning of intervals A and B were fast relative to the diffusion time constant for this sample. Therefore we chose this moment as time zero and analyzed the flow response relative to these strain steps. A one dimensional flow model using permeability of approximately 10^{-19} m^2, (see, for example, Morrow *et al.* (1986)) and 0.1% pore volume increase predicts a resaturation time of approximately 1 day. However, the experimental segments *A* and *B* showed slow but steady water influx after 2 days (Figures 6a and 7a). Consequently, we anticipate two stages in the resaturation process following each strain step: In the first stage the newly formed porosity in the sample is only partially saturated and water must diffuse in from the ends of the sample to resaturate the pore space. In the second stage, the sample has reached full saturation and additional fluid flow into the sample is the result of slow but continuous pore volume increase as new cracks open (*i.e.*, time-dependent creep at nearly constant stress). During this second stage, the influx of water provides an accurate measure of the long-term volumetric strain rate that occurred at the end of each loading segment. Observed flow rates at the end of strain steps *A* and *B* were $\Delta V/\Delta t$ = $1.9\text{x}10^{-6}$ cm^3/sec and $3.1\text{x}10^{-6}$ cm^3/sec, respectively (or volumetric strain rates of $2.2\text{x}10^{-9}$ sec^{-1} and $3.6\text{x}10^{-9}$ sec^{-1}).

Steady-state parallel flow through the sample is governed by Darcy's law:

$$\frac{q}{A} = -\frac{k}{\mu}\frac{dp}{dx} \tag{6}$$

where q is volumetric flow rate, k is permeability, μ is viscosity, A is cross-sectional area, dp is pore pressure change in the x-direction. Using conservation of mass and assuming incompressible flow results in the differential equation:

$$\frac{\partial^2 p}{\partial x^2} = \frac{\mu}{k}\frac{d\phi}{dt} \tag{7}$$

where ϕ is the sample porosity. Let λ be the position of the water front as measured from the end of the sample. Then for the case when the sample is not fully saturated ($\lambda < L/2$, where L is the length of the sample) we have the boundary conditions: $p|_{x=0} = p_0$ and $p|_{x=\lambda} = 0$ and the solution for differential equation (7) is:

$$\frac{dp}{dx} = \frac{\mu}{k}\frac{d\phi}{dt}\left(x - \frac{\lambda}{2}\right) - \frac{p_0}{\lambda} \quad . \tag{8a}$$

Once full saturation occurs, the center of the sample becomes a no-flow boundary and the solution to equation (7) is

$$\frac{dp}{dx} = \frac{\mu}{k}\frac{d\phi}{dt}\left(x - \frac{L}{2}\right) \quad . \tag{8b}$$

For the case where the sample is still saturating, combining (6) and (8a) gives expressions for the flow rate at the ends of sample

$$\left.\frac{q_0}{A}\right|_{x=0} = -\frac{\lambda}{2}\frac{d\phi}{dt} - \frac{k}{\mu}\frac{p_0}{\lambda} \tag{9}$$

and at the tip of the water front

$$\left.\frac{q_0}{A}\right|_{x=\lambda} = \frac{\lambda}{2}\frac{d\phi}{dt} - \frac{k}{\mu}\frac{p_0}{\lambda} \quad . \tag{10}$$

Therefore if sample porosity is constant (*i.e.,* $d\phi/dt = 0$) equation (8a) gives the analytical solution for the position of the water front:

$$\lambda(t) = \left[\frac{2kp_0t}{\mu\phi_0}\right]^{1/2} \tag{11}$$

where ϕ_0 is porosity, and t is time after application of the strain step. In case of a nonlinear change in sample porosity it is possible to solve equation (10) by an iterative technique, using the porosity history $\phi(t)$ as input.

In the case of constant volumetric strain (*i.e.,* $d\phi/dt = 0$), the pore pressure will drop linearly from the end of the sample to the saturation front and have a slope $dp/dx = p_0/\lambda$. A non-zero dilatancy rate will result in a curved pore pressure profile that departs from this constant slope. However, forward modeling with volumetric strain rate data recorded for strain steps *A* and *B*, as discussed in Appendix B, results in departures from linearity of less than 0.05 MPa.

Appendix B: Calculated Pore Volume and Sample Resaturation

We next calculate the pore volume change using recorded mechanical data. Total axial strain ε_x^{tot} is equal to the sum of elastic ε_x^{el} and inelastic ε_x^{inel} strain:

$$\varepsilon_x^{tot} = \frac{\Delta L}{L} = \varepsilon_x^{el} + \varepsilon_x^{inel} \tag{12}$$

where L is sample length. At constant confining pressure, elastic axial strain can be related to the applied differential stress σ_{dif} through the combined stiffness κ_0 of the sample and loading frame (Lockner, 1998)

$$\varepsilon_x^{el} = \frac{1}{L}\frac{\sigma_{dif}}{\kappa_0} \tag{13}$$

where $1/\kappa_0 = 1/\kappa_{\text{frame}} + 1/\kappa_{\text{sample}}$. For this loading frame and Westerly granite sample, measured stiffness is κ_0 = 129 MPa/mm. Our goal is to relate pore volume change (or volumetric strain) to measured quantities of axial stress and axial strain. The partial derivative $\partial\varepsilon_v^{inel} / \partial\varepsilon_x^{inel}$ will vary continuously from initial loading to sample failure. However, for a small increment of strain, we assume that pore volume change can be approximated as a linear function of inelastic axial strain:

$$\Delta V = AL\chi\varepsilon_x^{inel} = AL\chi\left(\varepsilon_x^{tot} - \frac{\sigma_{dif}}{L\kappa_0}\right) = A\chi\left(\Delta L - \frac{\sigma_{dif}}{\kappa_0}\right) \tag{14}$$

where A is the cross-sectional area of the sample and χ is a proportionality coefficient to be determined from the experimental data. Assuming that at the end of each loading stage the sample becomes fully saturated, then the pore volume change ΔV in equation (14) is equivalent to the recharge volume provided by the pore pressure pump. Under these conditions, (14) can be used to evaluate χ. Accordingly, we find that χ = 2.0 and 2.25 for strain steps *A* and *B* respectively. These values are reasonable for late-stage deformation of granite and the increase in χ from step *A* to *B*, reflecting increased dilatancy rate, is expected as the sample approaches failure.

An integration procedure was used to determine the position of the water front, using a time-stepping algorithm with 10 sec steps. For each step, the mechanical data were used (in equation 14) to determine the change in sample porosity:

$$\phi_{i+1} = \phi_i + \Delta\phi_i \quad . \tag{15}$$

We determined the position of the water front $\lambda\big|_{t=10\ sec}$ at the end of the first step according to equation (11) and then applied the iteration procedure calculating the flow rate of water q_i at the water front and the change in the position of the water at subsequent time steps using equations (7), (10) and (15) as follows:

$$\lambda_{i+1} = \lambda_i + \frac{\Delta t}{\phi_i}\left(\frac{k}{\mu}\frac{p_0}{\lambda_i} - \frac{1}{2}\frac{\Delta\phi_i}{\Delta t}\lambda_i\right) \quad . \tag{16}$$

Then we substitute the position of the water front into equation (9) and after integrating we have the total flux of water through the ends of the sample:

$$\Delta V = \int_0^t q\Big|_{x=0}\, dt \quad . \tag{17}$$

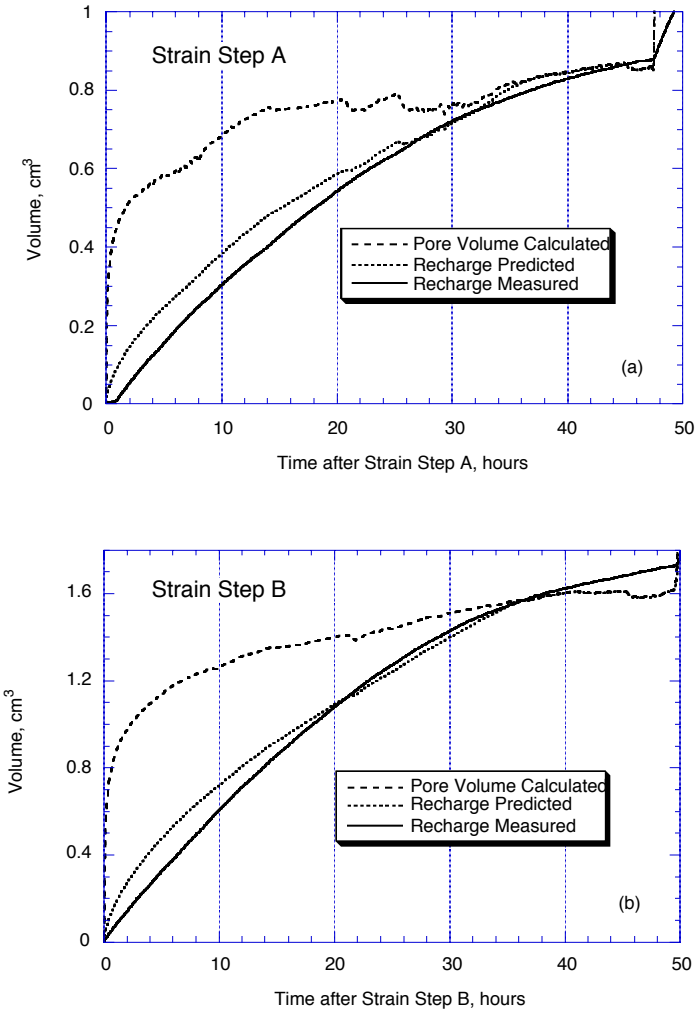

Figure 15. Calculated recharge and calculated pore volume change for strain steps *A* and *B* based on 1D diffusion model described in Appendix B. While the model provides a reasonably good match to the observed recharge rate, it over-predicts the early recharge. A more sophisticated 3D model would match the data better, but seems unnecessary for the present purposes. The model predicts that the resaturation front reaches the center of the sample after 36 hrs for both strain steps *A* and *B*.

We continue the iteration procedure until the water front reaches the center of the sample at which time the sample is fully saturated. After this time, additional water flows into the sample as needed to fill newly opened cracks. Following this procedure, the only parameter which is not determined directly from experimental measurements is permeability k. The iteration procedure of calculating pore volume according to (15) through (17) was made for different values of permeability. The optimum values of permeability were determined by matching the theoretical and observed pore fluid recharge curves (Figure 15), especially in the time interval between 20 and 40 hours. In this way, average permeabilities for flow in the axial direction were determined to be $k_A = 3.2 \times 10^{-20}$ m^2 and $k_B = 6.4 \times 10^{-20}$ m^2 for loading steps *A* and *B* respectively. Permeability of undeformed Westerly granite at

50 MPa effective confining pressure is approximately $6x10^{-20}$ m^2. The introduction of new microcracks at the beginning of step *B* apparently doubled the permeability.

The measured water recharge is compared to the calculated recharge and calculated pore volume change (based on equations (17) and (14) respectively) in Figures 15a and 15b. We find good agreement between measured and calculated flow rates for the late stages of each strain step (after about 20 hours). However in the initial stage of each test, the model we used tended to overestimate the water recharge. This difference is likely due to the model assumption that permeability is uniform throughout the sample. We have already noted (Figures 6 and 7) that velocity near the ends of the sample is higher than velocity in the sample center. This is due to lower microcrack density in the ends of the sample due to lateral support by the steel endcaps. The lower microcrack density should also result in lower permeability near the ends of the sample. Since pore water flow during the early stages of resaturation is restricted to the ends of the sample, the average permeability that we use in the recharge model will overestimate permeability during this stage. The more sophisticated modeling needed to correct of permeability heterogeneity does not seem warranted. The simple 1D model developed here provides a reasonable approximation of the observed recharge rate and gives useful information regarding resaturation time, position of the resaturation front and average permeability. Full resaturation of the sample was estimated to occur 36.0 and 35.7 hours after strain steps *A* and *B* respectively.

We showed in Appendix A that the assumption of incompressible flow leads to a simple analytic form (equation (8a)) for the pressure gradient in the sample. If volumetric strain is constant, the pressure gradient is constant from the sample end to the saturation front. For homogeneous volumetric strain rate, the pressure gradient varies linearly from the sample end to the resaturation front. This implies that the pore pressure profile at any given time will be parabolic (concave upward). Forward modeling using the observed recharge rates results in pressure profiles that are within 0.05 MPa of the linear profile predicted for $d\phi/dt = 0$.

Once the resaturation fronts meet at the center, symmetry requires that the central plane of the sample be a no-flow boundary. In this case, the pressure gradient is given by equation (8b). For $d\phi/dt = 0$, the pressure gradient is zero throughout the sample and $p = p_0$ everywhere. For homogeneous volumetric strain rate, pore pressure drops to a minimum at the center of the sample. Using the observed recharge rates and the permeabilities estimated in the modeling, the pressure drop at the center of the sample was 0.31 MPa and 0.26 MPa at the end of strain steps *A* and *B*, respectively.

Acknowledgements. We thank B. Kilgore and E. Roeloffs for numerous helpful suggestions in improving this manuscript. This research was supported by the National Earthquake Hazards Reduction Program.

References

Aggarwal, Y. P., L. R. Sykes, J. Armbruster, and M. L. Sbar (1973). Premonitory changes in seismic velocities and prediction of earthquakes, *Nature*, **241**, 101-104.

Andrews, D. J. (2003). A fault constitutive relation accounting for thermal pressurization of pore fluid, *J. Geophys. Res.*, **107**, 2363, 10.1029/2002JB001942R.

Barsukov, O. M. (1970). On correlation of rock electric resistivity and tectonic processes, *Izv. An. USSR, Fizika Zemli*, **1**, 84-89.

Biot, M. A. (1956). Theory of propagation of elastic waves in a fluid-saturated porous solid I. Low-frequency range, II. High frequency range, *J. Acoust. Soc. Amer.*, **28**, N2, 168-191.

Blair, D. P. (1990). A direct comparison between vibrational resonance and pulse transmission data for assessment of seismic attenuation in rocks, *Geophys.*, **55**, 51-60.

Blanpied, M. L., D. A. Lockner, and J. D. Byerlee (1992). An earthquake mechanism based on rapid sealing of faults, *Nature*, **358**, 574-576.

Bonner, B. P. (1974). Shear wave birefringence in dilating granite, *Geophys. Res. Lett.*, **1**, 5, 217-220.

Brace, W. F., B. W. Paulding, and C. Scholz (1966). Dilatancy in the fracture of crystalline rocks, *J. Geophys. Res.*, **71**, 3939-3953.

Byerlee, J. D., and D. A. Lockner (1977). Acoustic emission during fluid injection in rock, in *Proceedings, First Conference on Acoustic Emission/Microseismic Activity in Geological Structures and Materials*, eds. (Hardy, H. R., and F. W. Leighton), Trans Tech Publications, Clausthal-Zellerfeld, Germany, 87-98.

Cadoret, T., D. Marion, and B. Zinszner (1995). Influence of frequency and fluid distribution on elastic wave velocities in partially saturated limestones, *J. Geophys. Res.*, **100**, 9789-9803.

Dubendorf, B., and W. Menke (1986). Time-domain apparent-attenuation operators for compressional and shear waves: experiment versus single scattering theory, *J. Geophys. Res.*, **91**, 14023-14032.

Dvorkin, J., and A. Nur (1993). Dynamic poroelasticity: A unified model with the squirt and the Biot mechanisms, *Geophys.*, **58**, 524-533.

Hadley, K. (1976). Comparison of calculated and observed crack densities and seismic velocities in Westerly granite, *J. Geophys. Res.*, **81**, 20, 3484-3494.

Johnston, M. J. S., and A. T. Linde (2002). Implications of crustal strain during conventional, slow, and silent earthquakes, in *International Handbook of Earthquake and Engineering Seismology*, eds. (Lee, W. H. K., H. Kanamori, P. C. Jennings, and C. Kisslinger), Academic Press, Amsterdam, 589-605.

Johnston, M. J. S., A. T. Linde, and M. T. Gladwin (1990). Near-field high resolution strain measurements prior to the October 18, 1989, Loma Prieta M_s 7.1 Earthquake, *Geophys. Res. Lett.*, **17**, 10, 1777-1780.

Johnston, M. J. S., A. T. Linde, M. T. Gladwin, and R. D. Borcherdt (1987). Fault failure with moderate earthquakes, *Tectonophysics*, **144**, 189-206.

Kranz, R. L. (1980). The effects of confining pressure and stress difference on static fatigue of granite, *J. Geophys. Res.*, **85**, B4, 1854-1866.

Kranz, R. L., T. Satoh, O. Nishizawa, K. Kusunose, M. Takahashi, K. Masuda, and A. Hirata (1990). Laboratory study of fluid pressure diffusion in rock using acoustic emissions, *J. Geophys. Res.*, **95**, B13, 21593-21607.

Kranz, R. L., and C. H. Scholz (1977). Critical dilatant volume of rocks at the onset of tertiary creep, *J. Geophys. Res.*, **82**, 30, 4893-4898.

Lachenbruch, A. H. (1980). Frictional heating, fluid pressure, and the resistance to fault motion, *J. Geophys. Res.*, **85**, B11, 6097-6112.

Li, Y. G., and J. E. Vidale (2001). Healing of the shallow fault zone from 1994-1998 after the 1992 *M*7.5 Landers, California, earthquake, *Geophys. Res. Lett.*, **28**, 2999-3002.

Linde, A. T., and M. J. S. Johnston (1989). Source parameters of the October 1, 1987 Whittier Narrows earthquake from crustal deformation data, *J. Geophys. Res.*, **94**, 9633-9643.

Lindh, A. G., D. A. Lockner, and W. H. K. Lee (1978). Velocity anomalies: an alternative explanation, *Bull. of the Seism. Soc. of Amer.*, **68**, 3, 721-734.

Lockner, D. A. (1993a). The role of acoustic emission in the study of rock fracture, *Int. J. Rock Mech. Min. Sci. Geomech. Abstr.*, **30**, 7, 883-899.

Lockner, D. A. (1993b). Room temperature creep in saturated granite, *J. Geophys. Res.*, **98**, B1, 475-487.

Lockner, D. A. (1998). A generalized law for brittle deformation of Westerly granite, *J. Geophys. Res.*, **103**, B3, 5107-5123.

Lockner, D. A., and J. D. Byerlee (1977). Acoustic emission and creep in rock at high confining pressure and differential stress, *Bull. of the Seismological Society of Amer.*, **67**, 2, 247-258.

Lockner, D. A., and J. D. Byerlee (1978). Velocity anomalies: an alternative explanation based on data from laboratory experiments, *Pure and Applied Geophys.*, **116**, 765-772.

Lockner, D. A., and J. D. Byerlee (1980). Development of fracture planes during creep in granite, in *Proceedings, Second Conference on Acoustic Emission/Microseismic Activity in Geological Structures and Materials*, eds. (Hardy, H. R., and W. F. Leighton), Trans-Tech Publications, Clausthal-Zellerfeld, Germany, 11-25.

Lockner, D. A., and J. D. Byerlee (1994). Dilatancy in hydraulically isolated faults and the suppression of instability, *Geophys. Res. Lett.*, **21**, 22, 2353-2356.

Lockner, D. A., and J. D. Byerlee (1995). An earthquake instability model based on faults containing high fluid-pressure compartments, *Pure Appl. Geophys.*, **145**, 2/3, 717-745.

Lockner, D. A., J. D. Byerlee, V. Kuksenko, A. Ponomarev, and A. Sidorin (1991). Quasi-static fault growth and shear fracture energy in granite, *Nature*, **350**, 39-42.

Lockner, D. A., J. D. Byerlee, V. Kuksenko, A. Ponomarev, and A. Sidorin (1992a). Observations of quasistatic fault growth from acoustic emissions, in *Fault Mechanics and Transport Properties of Rocks*, eds. (Evans, B., and T.-f. Wong), Academic Press, London, 3-31.

Lockner, D. A., M. J. S. Johnston, and J. D. Byerlee (1983). A mechanism for the generation of earthquake lights, *Nature*, **302**, 28-33.

Lockner, D. A., D. E. Moore, and Z. Reches (1992b). Microcrack interaction leading to shear fracture, in *33rd U.S. Rock Mechanics Symposium*, eds. (Tillerson, J. R., and W. R. Wawersik), Balkema, A. A., Rotterdam, 807-816.

Lockner, D. A., and S. Stanchits (2002 in press). Poroelastic response of sandstones to deviatoric stress change, *J. Geophys. Res.*

Lockner, D. A., J. B. Walsh, and J. D. Byerlee (1977). Changes in seismic velocity and attenuation during deformation of granite, *J. Geophys. Res.*, **82**, 33, 5374-5378.

Madden, T. R. (1983). Microcrack connectivity in rocks: a renormalization group approach to the critical phenomena of conduction and failure in crystalline rocks, *J. Geophys. Res.*, **88**, 585-592.

Masuda, K., O. Nishizawa, K. Kusunose, and T. Satoh (1993). Laboratory study of effects of in situ stress state and strength on fluid-induced seismicity, *Int. J. Rock Mech. Min. Sci. & Geomech. Abstr.*, **30**, 1, 1-10.

Masuda, K., O. Nishizawa, K. Kusunose, T. Satoh, M. Takahashi, and R. Kranz (1990). Positive feedback fracture process induced by nonuniform high-pressure water flow in dilatant granite, *J. Geophys. Res.*, **95**, B13, 21583-21592.

Mavko, G., T. Mukerji, and J. Dvorkin (1998). *The Rock Physics Handbook: Tools for Seismic Aalysis in Porous Media*, Cambridge University Press, Cambridge, 329 p.

Mavko, G., T. Mukerji, and N. Godfrey (1995). Predicting stress-induced velocity anisotropy in rocks, *Geophys.*, **60**, 1081-1087.

Mavko, G., and A. Nur (1975). Melt squirt in asthenosphere, *J. Geophys. Res.*, **80**, 1444-1448.

Mavko, G., and A. Nur (1979). Wave attenuation in partially saturated rocks, *Geophys.*, **44**, 161-178.

Menke, W., D. Witte, and R. Chen (1984). Laboratory test of apparent attenuation formulas, *Bull. Seismol. Soc. Amer.*, **74**, 1079-1081.

Miller, S. A., A. Nur, and D. L. Olgaard (1996). Earthquakes as a coupled shear stress - high pore pressure dynamical system, *Geophys. Res. Lett.*, **23**, 2, 197-200.

Moore, D. E., and D. A. Lockner (1995). The role of microcracking in shear-fracture propagation in granite, *J. Struct. Geol.*, **17**, 95-114.

Morrow, C. A., Z. Bo-Chong, and J. D. Byerlee (1986). Effective pressure law for permeability of Westerly granite under cyclic loading, *J. Geophys. Res.*, **91**, 3870-3876.

Nur, A. (1972). Dilatancy, pore fluids, and premonitory variations of t_s/t_p travel times, *Bull. Seismol. Soc. Am.*, **62**, 1217-1222.

Nur, A., and G. Simmons (1969). Stress-induced velocity anisotropy in rock: An experimental Study, *J. Geophys. Res.*, **74**, 27, 6667-6674.

Robinson, R. R., R. L. Wesson, and W. L. Ellsworth (1972). Variation of P-wave velocity before the Bear Valley, California earthquake of February 24, 1972, *Science*, **184**, 1281-1283.

Scholz, C. H. (1968a). Mechanism of creep in brittle rock, *J. Geophys. Res.*, **73**, 3295-3302.

Scholz, C. H. (1968b). Microfracturing and the inelastic deformation of rock in compression, *J. Geophys. Res.*, **73**, 1417-1432.

Scholz, C. H., L. R. Sykes, and Y. P. Aggarwal (1973). Earthquake prediction: a physical basis, *Science*, **181**, 803-810.

Semyonov, A. N. (1969). A change in ratio of transverse to longitudinal waves travel time before strong shocks, *Izv. An. USSR, Fizika Zemli*, **4**, 72-77.

Sibson, R. H. (1973). Interactions between temperature and pore-fluid pressure during earthquake faulting and a mechanism for partial or total stress relief, *Nature*, **243**, 66-68.

Sobolev, G. A. (1995). *Fundamentals of Earthquake Prediction*, Electromagnetic Research Center, Moscow?

Tapponnier, P., and W. F. Brace (1976). Development of stress-induced microcracks in Westerly granite, *Int. J. Rock Mech. Min. Sci. & Geomech. Abstr.*, **13**, 103-112.

Whitcomb, J. H., J. D. Garmany, and D. L. Anderson (1973). Earthquake prediction: Variation of seismic velocities before the San Fernando earthquake, *Science*, **180**, 632-635.

Yanagidani, T., S. Ehara, O. Nishizawa, K. Kusunose, and M. Terada (1985). Localization of dilatancy in Ohshima granite under constant uniaxial stress, *J. Geophys. Res.*, **90**, 6840-6858.

Yukutake, H. (1989). Fracturing process of granite inferred from measurements of spatial and temporal variations in velocity during triaxial deformations, *J. Geophys. Res.*, **94**, 15639-15651.

Yukutake, H. (1992). Fracture nucleation process in intact rocks, *Tectonophys.*, **211**, 247-257.

Zoback, M. D., and J. D. Byerlee (1975). The effect of microcrack dilatancy on the permeability of Westerly granite, *J. Geophys. Res.*, **80**, 5, 752-755.